The Astrophysical Journal, 980:59 (14pp), 2025 February 10 https://doi.org/10.3847/1538-4357/ada4ac

Do Unusually Cold Starburst Galaxies Exist? A Case Study

Dominik A. Riechers
Institut für Astrophysik, Universität zu Köln, Zülpicher Straße 77, D-50937 Köln, Germany; riechers@ph1.uni-koeln.de
Received 2024 January 10; revised 2024 December 23; accepted 2024 December 30; published 2025 February 4

Abstract

We report observations of CO($J = 9 \rightarrow 8$) and OH^+($N = 1 \rightarrow 0$) toward the four millimeter-selected lensed starburst galaxies SPT 2354−58, 0150−59, 0314−44, and 0452−50, using the Atacama Large Millimeter/submillimeter Array (ALMA) Atacama Compact Array, as part of a larger study of OH^+ in the early Universe. In this work, we use these observations for the main purpose of spectroscopic redshift measurements. For all sources except SPT 0452−50, we confirm the previously reported most likely redshifts, and we find typical CO and OH^+ properties for massive starbursts. For SPT 0452−50, we rule out the previously reported value of $z = 2.0105$, measuring a firm redshift of $z = 5.0160$ based on [O I], [C II], H_2O, and CO emission instead when adding in ancillary ALMA data. Previously, SPT 0452−50 was considered an outlier in relations between dust temperature, far-infrared luminosity, and redshift, which may have hinted at an unusually cold starburst with a dust temperature of only $T_{\rm dust} = (21 \pm 2)$ K. Instead, our new measurements suggest it to be among highly luminous massive dusty starbursts at $z > 5$, with rather typical properties within that population. We find a revised dust temperature of $T_{\rm dust} = (76.2 \pm 2.5)$ K, and an updated lensing-corrected far-infrared luminosity (42.5–122.5 μm) of $(2.35^{+0.09}_{-0.08}) \times 10^{13}\,L_\odot$, i.e., about an order of magnitude higher than previously reported. We thus do not find evidence for the existence of unusually cold starburst galaxies in the early Universe that were missed by previous selection techniques.

Unified Astronomy Thesaurus concepts: Active galaxies (17); Galaxy evolution (594); Starburst galaxies (1570); High-redshift galaxies (734); Infrared excess galaxies (789); Interstellar line emission (844); Interstellar line absorption (843); Submillimeter astronomy (1647); Millimeter astronomy (1061)

1. Introduction

Massive dusty starburst galaxies, also commonly labeled "dusty star-forming galaxies" (DSFGs), are an important ingredient to our understanding of massive galaxy evolution across cosmic history, because they represent such systems in their most active phases of growth (see A. W. Blain et al. 2002; J. A. Hodge & E. da Cunha 2020 for reviews). While dust has now been detected in relatively "normal" galaxies back to $z > 8$ (e.g., Y. Tamura et al. 2019), the space density of DSFGs appears to drastically decrease toward $z > 5$, with just over 20 spectroscopically confirmed systems at $z = 5$–6 extracted from surveys extending over thousands of square degrees on the sky, four at $z = 6$–7, and none at earlier epochs (D. A. Riechers et al. 2010, 2013, 2014, 2017, 2020, 2021b; F. Combes et al. 2012; F. Walter et al. 2012; A. Weiß et al. 2013; M. L. Strandet et al. 2016, 2017; Y. Fudamoto et al. 2017; R. Pavesi et al. 2018; J. A. Zavala et al. 2018; S. Jin et al. 2019; C. Reuter et al. 2020; S. Ikarashi et al. 2022; P. Cox et al. 2023; I. Mitsuhashi et al. 2024). This is one of the reasons why redshift completeness for systematically selected samples of DSFGs is important, in order to not miss rare $z > 5$ specimens with potentially unusual dust properties.

While rare, the DSFG population reaches enormous bolometric luminosities, which are typically dominantly transmitted at long wavelengths due to dust obscuration. They thus exhibit far-infrared luminosities of $L_{\rm FIR} \sim 0.4$–$3 \times 10^{13}\,L_\odot$, indicative of starbursts in excess of ~$500\,M_\odot\,{\rm yr}^{-1}$, which are sometimes further flux boosted by up to an order of magnitude or more by gravitational lensing (e.g., Y. D. Hezaveh et al. 2013; T. D. Rawle et al. 2014; J. S. Spilker et al. 2016; Y. Fudamoto et al. 2017; D. A. Riechers et al. 2020). Due to these intense starbursts, the dust in DSFGs is typically relatively warm, but it has been subject to debate whether or not they are warmer than other star-forming galaxy populations (since high dust optical depths may cause the warmest dust to be hidden), whether or not their dust temperatures $T_{\rm dust}$ evolve with redshift, or if there is evidence for a general evolution toward warmer dust in star-forming galaxies with increasing redshift, which goes beyond the heating contribution from the increasingly warmer cosmic microwave background (CMB; e.g., B. Magnelli et al. 2014; C. Schreiber et al. 2018; U. Dudzevičiūtė et al. 2020; D. A. Riechers et al. 2020).

The high levels of activity in DSFGs, combined with their high observable brightness, provides access to a suite of diagnostic tools which are often not accessible beyond the local Universe. Of particular interest are diagnostic lines such as the high-rotational levels of CO which hold information about the gas excitation mechanisms associated with the starbursts (see C. L. Carilli & F. Walter 2013 for a review), and light hydrides as tracers of the diffuse gas associated with infalling material or large-scale outflows. A particularly promising tool in this regard are the ground-state rotational levels of the highly reactive OH^+ molecular ion, which is thought to show enhanced abundances in diffuse atomic gas subjected to high cosmic-ray fluxes, such as expected in gas flows bathed in the radiation fields created by intense starbursts (e.g., D. Hollenbach et al. 2012).[1]

[1] There are three such levels: OH^+ $N_J = 1_0 \rightarrow 0_1$, $N_J = 1_2 \rightarrow 0_1$, and $N_J = 1_1 \rightarrow 0_1$, with their strongest components at rest frequencies of 909.1588, 971.8053, and 1033.058 GHz, respectively.

Consequently, OH^+ absorption has now been detected in >20 high-z massive starbursts (e.g., D. A. Riechers et al. 2013, 2021a, 2021b; N. Indriolo et al. 2018; S. Berta et al. 2021; K. M. Butler et al. 2021), which makes it possible to start investigating statistical properties.

As an extension of this study, we thus have targeted an additional ~70 high-z massive starbursts in at least one ground-state OH^+ transition, which also provided simultaneous coverage of the CO($J = 9 \rightarrow 8$) transition in all cases (D. Riechers et al. 2025, in preparation). This sample includes galaxies from the South Pole Telescope (SPT) survey of DSFGs (J. D. Vieira et al. 2010). As a byproduct, this study has allowed us to independently confirm the redshifts of three sources in this survey which could still have been considered ambiguous based on previous studies (A. Weiß et al. 2013; M. L. Strandet et al. 2016; C. Reuter et al. 2020). We thus report on the outcome of these observations here, in the interest of the redshift completeness of the sample. In addition, we failed to detect both targeted lines in one source in the entire sample, which was also selected from the SPT survey. Given the potentially unusual nature of this source, we here provide an in-depth analysis of this source, including a range of revised properties.

We present the sample, data, and calibration in Section 2, before presenting the outcome of the observations in Section 3 and the deeper analysis in Section 4. A brief summary and conclusions are provided in Section 5. We use a concordance, flat Lambda cold dark matter (ΛCDM) cosmology throughout, with $H_0 = 69.6$ km s^{-1} Mpc^{-1}, $\Omega_M = 0.286$, and $\Omega_\Lambda = 0.714$.

2. Data

2.1. Sample Selection

The four targets analyzed in this work are selected from the SPT survey of bright DSFGs (C. Reuter et al. 2020 and references therein), and from a larger survey of high-z starbursts targeting the $OH^+(N_J = 1_1 \rightarrow 0_1)$ line for which the first results were reported by D. A. Riechers et al. (2021a). The first three targets are included here with the main purpose of unambiguously confirming their spectroscopic redshifts, as a byproduct of the OH^+ survey.[2]

The fourth target, SPT 0452−50, is included here because the observations targeting OH^+ called its redshift identification into question, as described in more detail in the following. Despite being only a single source, its analysis is of particular interest in the context of discussions of T_{dust}–z relations, since any such relations depend on the underlying galaxy selection function. For dusty galaxies with well-sampled dust spectral energy distributions (SEDs), the uncertainties in parameters for individual sources in general are relatively minor, such that even rare outliers can have an impact on perceived relations. As shown in Figure 8 of C. Reuter et al. (2020), SPT 0452−50 was found to be a far outlier in the T_{dust}–L_{FIR}–z parameter space (see also M. L. Strandet et al. 2016), suggesting that it could be an unusually cold massive starburst with a dust temperature of only $T_{dust} = 21 \pm 2$ K (the rest of their sample all have $T_{dust} > 30$ K). SPT 0452−50 would also be an outlier in T_{dust} in other DSFG samples with well-measured dust SEDs. As an example, D. Ismail et al. (2023) report T_{dust} for 125 Herschel-selected DSFGs at $z = 1.4$–5.4, which at face value show individual values as low as $20.5^{+2.8}_{-2.0}$ K. However, these values are determined based on optically thin SED fits, which the same authors find to underpredict T_{dust} by 5–15 K compared to general SED fits that account for dust optical depth effects.[3] As such, no sources as cold as SPT 0452−50 appear to be found in broader DSFG samples when accounting for differences in SED fitting methods. Such sources may be rare in current samples, because some selection techniques to identify high-z massive starbursts may actively select against such sources. Should they exist in considerable quantities, they could substantially alter our understanding of T_{dust}–z relations in the early Universe. As such, this source is analyzed here in greater detail.

2.2. New ALMA/ACA Observations

We observed the redshifted CO($J = 9 \rightarrow 8$) and $OH^+(N_J = 1_1 \rightarrow 0_1)$ lines ($\nu_{rest} = 1036.9124$ and 1033.0582 GHz) toward the four galaxies in our sample in Bands 6 and 7 with the Atacama Large Millimeter/submillimeter Array (ALMA) Atacama Compact Array (ACA), using nine or ten 7 m antennas covering 8.9–48.9 m baselines (see Table 1). For two galaxies, the observing setups also covered the $OH^+(N_J = 1_2 \rightarrow 0_1)$ line ($\nu_{rest} = 971.8053$ GHz). Observations were carried out in cycle 8 under good to excellent weather conditions between 2022 March 31 and July 29 (project ID: 2021.2.00062.S; PI: Riechers), spending between 19 and 22 minutes on source per target. We also observed a second, lower Band 7 setup for SPT 0452−50 with the ALMA/ACA for 25 minutes in cycle 10 on 2023 December 17 (project ID: 2023.1.01481.S; PI: Riechers). Radio quasars close to the sources in sky projection were observed for complex gain, bandpass, and absolute flux calibration (see Table 1; the bandpass and flux calibrators were identical where not listed separately). The absolute flux calibration is estimated to be reliable to within <10%.

The ACA correlator was set up with two spectral windows of 1.875 GHz bandwidth (dual polarization) each per sideband, at a sideband separation of typically 8 GHz. A spectral resolution of 31.25 MHz at a channel spacing of 15.625 MHz was chosen for all observations to reduce calibration overheads. Thus, neighboring channels in spectra shown at full resolution are not independent.

All data were calibrated aided by the calibration pipeline in `CASA` version 6.2.1 (J. P. McMullin et al. 2007), and manually imaged using the CLEAN algorithm via the `tclean` task with "natural" baseline weighting, resulting in the synthesized beam sizes listed in Table 1. This is with the exception of the second Band 7 observations, where `CASA` version 6.5.4 was used for calibration. The 2022 (2023) data for SPT 2354−58, 0150−59, 0314−44, and 0452−50 reach rms noise levels of 8.5/9.3, 2.6/3.2, 3.7/4.4, and 6.0/6.4 (4.1/5.8) mJy beam^{-1} per 15.625 MHz channel in the lower/upper sideband (LSB/USB), respectively.

[2] These sources were reported as single-line CO detections in the survey by C. Reuter et al. (2020), which results in ambiguous redshift identifications in at least two cases. The redshift of SPT 2354–58 was previously determined based on a CO($J = 4 \rightarrow 3$) emission line and an absorption line identified as $OH^+(N_J = 1_2 \rightarrow 0_1)$. For lensed galaxies, there is a chance that absorption lines can be associated with the foreground lensing galaxies (or other interlopers). While unlikely, we here include this source among those confirmed for completeness.

[3] Fitting their coldest source, HELMS35, with a general SED fit following the method described below yields $T_{dust} = 41.9^{+1.7}_{-3.9}$ K.

Table 1
ALMA Observations

SPT Name	LSB/USB Center (GHz)	Band	N_{ant}	$\theta_{maj} \times \theta_{min}$[a]	Observing Dates	t_{on} (minutes)	Complex Gain Calibrator	Bandpass/Flux Calib.[†]
ALMA/ACA (1.8 hr)[b]								
2354−58 (J2354−5815)	348.85/360.77	7	9	5.″4 × 3.″5/6.″4 × 3.″2	2022 Mar 31	22.2	J2357−5311	J2253+1608
0150−59 (J0150−5924)	257.45/272.82	6	9	7.″1 × 4.″8/6.″7 × 4.″5	2022 Apr 12	19.2	J0210−5101	J2253+1608
0314−44 (J0314−4452)	248.88/262.59	6	9	6.″2 × 4.″9/5.″9 × 4.″6	2022 Jul 29	21.2	J0334−4008	J0538–4405
0452−50 (J0452−5018)	331.55/343.45	7	10	5.″0 × 3.″4/4.″8 × 3.″4	2022 May 21	19.7	J0515−4556	J0538–4405
	304.84/316.75	7	10	6.″3 × 3.″3/6.″0 × 3.″2	2023 Dec 17	25.2	J0515−4556	J0538–4405
Archival data (2.6 hr)[b]								
0452−50	254.08/267.93	6	10	6.″9 × 4.″4/6.″5 × 4.″2	2019 Oct 3 and 13	58.8	J0455−4615	J0538–4405
	162.56/174.56	5	10	10.″3 × 6.″6/9.″6 × 6.″3	2019 Nov 10	94.9	J0455−4615	J0538–4405
Literature data (3 minutes)[b]								
0452–50	97.29/109.29	3	15[c]	6.″5 × 5.″6/5.″8 × 5.″0	2011 Nov 19	3.0	J0455−4615	J0538–4405 Mars[†]

Notes. For clarity of identification, the "†" symbol indicates which source is the flux calibrator.
[a] Synthesized beam size.
[b] Total on-source time t_{on}.
[c] Observations using the 12 m antennas in the main array. All other cases are the ACA 7 m antennas.

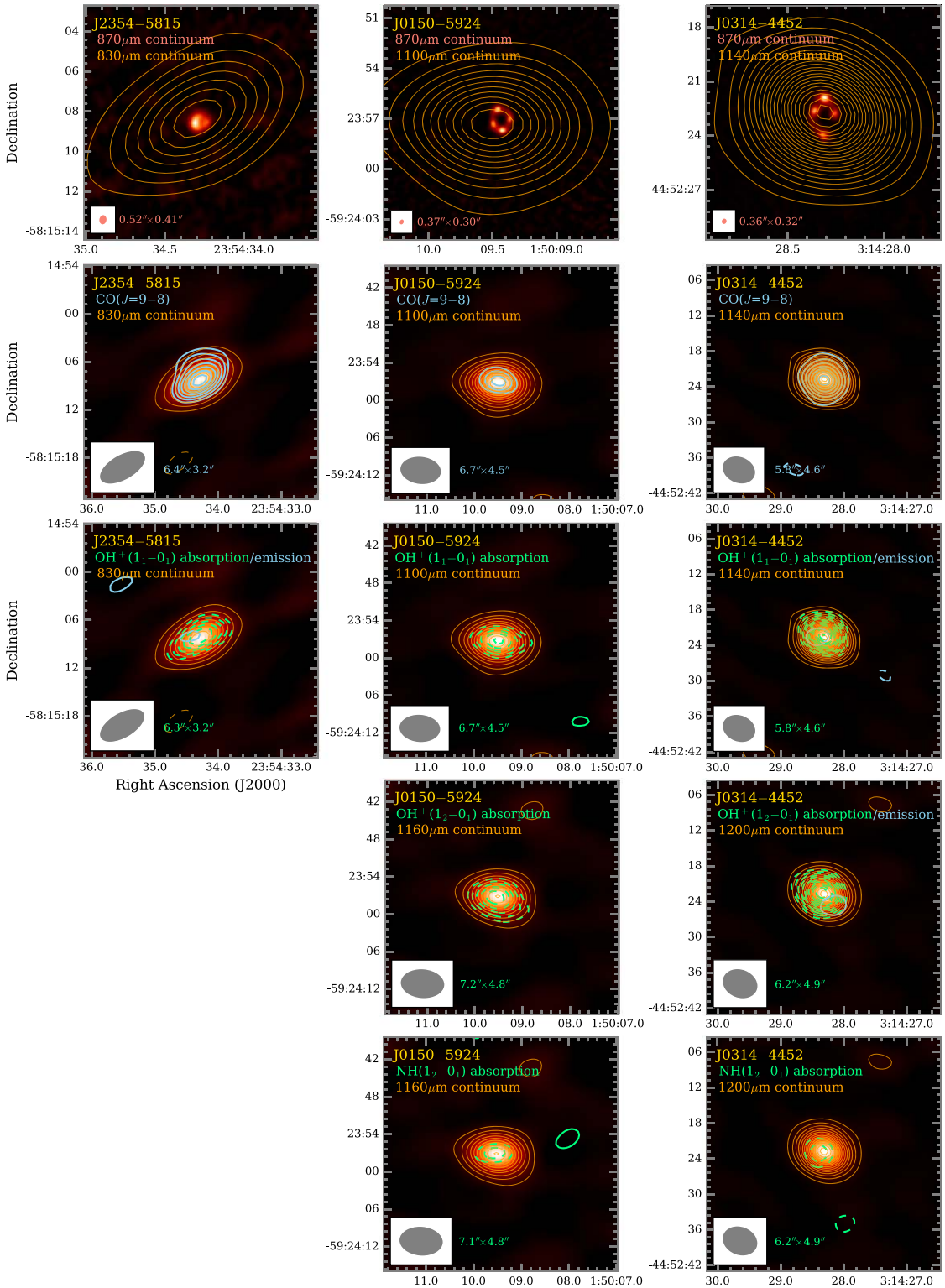

Figure 1. Line and continuum emission toward SPT 2354−58, 0150−59, and 0314−44 (left to right). Top row: USB continuum contours overlaid on archival ALMA 870 μm high-resolution continuum images (project IDs: 2011.0.00958.S, 2016.1.00231.S, and 2019.1.01026.S, respectively; left background data previously published by J. S. Spilker et al. 2016). Second and third rows: CO($J = 9 \rightarrow 8$) and OH$^+$($N_J = 1_1 \rightarrow 0_1$) emission/absorption contours overlaid on USB continuum emission and contours. Fourth and fifth rows: OH$^+$ and NH $N_J = 1_2 \rightarrow 0_1$ emission/absorption contours overlaid on LSB continuum emission and contours. Continuum contours (orange) are shown in steps of $\pm 3\sigma$, where $1\sigma = 0.67$ and 1.14 (2.3, 0.68, and 0.95) mJy beam^{-1} in the LSB (USB; always ordered left to right). Line contours are shown in steps of 1σ, starting at $\pm 3\sigma$, except for SPT 0314–44, where CO($J = 9 \rightarrow 8$) is shown in steps of 2σ. For the second row, $1\sigma = 2.8$, 1.1, and 1.3 mJy beam^{-1}, respectively. For the third row, $1\sigma = 3.8$, 1.2, and 1.3 (2.3, N/A, and 1.5) mJy beam^{-1} for absorption (emission), respectively. For the fourth row, $1\sigma = 1.0$ and 1.6 (N/A and 1.7) mJy beam^{-1} for absorption (emission), respectively. For the fifth row, $1\sigma = 0.80$ and 1.8 mJy beam^{-1}, respectively. Negative contours are dashed. Observed-frame continuum wavelengths are indicated in each panel. The synthesized beam size is indicated in the bottom-left corner of each panel.

Table 2
Continuum Fluxes

SPT 2354−58		SPT 0150−59		SPT 0314−44		SPT 0452−50	
ν_{obs} (GHz)	Flux (mJy)	ν_{obs} (GHz)	Flux (mJy)	ν_{obs} (GHz)	Flux (mJy)	ν_{obs} (GHz)	Flux (mJy)
349	65.6 ± 2.3	257	20.28 ± 0.67	249	58.2 ± 1.1	97	0.71 ± 0.17
361	67.1 ± 2.8	273	24.23 ± 0.68	263	65.1 ± 0.9	109	1.61 ± 0.23
						163	6.11 ± 0.18
						175	8.41 ± 0.23
						254	23.73 ± 0.38
						268	27.26 ± 0.39
						305	37.17 ± 0.81
						317	38.15 ± 0.98
						332	41.24 ± 0.84
						343	43.26 ± 0.97

2.3. Archival ALMA/ACA Observations

We also include archival cycle 7 ALMA/ACA Band 5 and 6 observations targeting the two [C I] fine-structure lines in SPT 0452−50 at the redshift of $z = 2.011$ reported by C. Reuter et al. (2020) during two observing runs each (project ID: 2019.1.00297.S; PI: Bethermin). The details of these observations are provided in Table 1. The correlator setups are the same as those in the previous subsection, except for the tuning frequencies, and that a 2 times higher spectral resolution (i.e., 7.8125 MHz) was chosen for the spectral windows expected to contain the lines (one in Band 5, two in Band 6). All data were calibrated aided by the calibration pipeline in CASA version 6.2.1, and manually imaged. The Band 5 (Band 6) data reach rms noise levels of 1.5/2.4 (4.4/4.1) mJy beam^{-1} per 15.625 MHz channel in the LSB/USB, respectively.

2.4. Literature ALMA Observations

For our analysis, we have also recalibrated one of the cycle 0 ALMA 12 m Band 3 observations of SPT 0452−50 previously published by A. Weiß et al. (2013; project ID: 2011.0.00957.S; PI: Weiß). These observations were part of the line scan observations used to determine its redshift, and reported to contain no line emission. The details of these observations are provided in Table 1. The correlator setups are the same as those in the previous subsection, except for the tuning frequencies, and that a spectral resolution of 488.281 kHz was utilized. In addition, due to the poorly known flux scales of many flux calibrators at the time, Mars was observed for flux calibration. The data and calibration procedures were edited to be compatible with current versions of CASA, and to reduce the excessive edge channel flagging applied by default versions of the calibration. All data were then calibrated aided by the calibration pipeline in CASA version 6.2.1 and manually imaged, achieving an rms noise level of 2.6 mJy beam^{-1} per 15.625 MHz channel in the LSB.

3. Results

3.1. Confirmed Sources

We successfully detect rest-frame 290 μm continuum emission toward SPT 2354−58, 0150−59, and 0314−44 (Figure 1). The peak significance of the detections in the lower (upper) sidebands is 31, 30, and 47σ (23, 36, and 64σ), respectively. The emission is marginally resolved at best and smaller than the beam size in all cases, consistent with the modest sizes of the strongly lensed galaxies in high-resolution ALMA images. Continuum fluxes were extracted from two-dimensional Gaussian fitting in the image plane.[4] All continuum fluxes are reported in Table 2. To investigate the presence of emission and absorption lines, continuum emission was subtracted from all data cubes in the visibility plane, excluding spectral regions of potential lines in the fitting process. The subtraction accounts for the spectral slope of the continuum where measurable within the line-free spectral ranges.

We detect CO($J = 9 \rightarrow 8$) emission at 9.5, 5.4, and 16σ peak significance and $OH^+(N_J = 1_1 \rightarrow 0_1)$ absorption at 7.9, 7.2, and 16σ peak significance toward SPT 2354−58, 0150−59, and 0314−44, respectively (Figure 1). We also detect $OH^+(N_J = 1_2 \rightarrow 0_1)$ absorption at 7.7 and 14σ peak significance and $NH(N_J = 1_2 \rightarrow 0_1)$ absorption at 4.6 and 4.6σ peak significance toward SPT 0150−59 and 0314−44, respectively. The emission components of $OH^+(N_J = 1_1 \rightarrow 0_1)$ are tentatively detected at 3.3 and 3.7σ peak significance toward SPT 2354−58 and 0314−44, respectively. The emission component of $OH^+(N_J = 1_2 \rightarrow 0_1)$ is also tentatively detected at 3.9σ peak significance toward SPT 0314–44. Those OH^+ lines seen in emission are detected as inverse P-Cygni profiles, which is consistent with what is expected for outflowing gas (Figure 2 and Table 3).[5] In SPT 2354−58, the OH^+ absorption is slightly redshifted, while in the other two galaxies, the centroid velocities are consistent with the systemic redshift within <1–2σ. Given the broad CO line widths compared to the shifts, the absorption components alone thus do not conclusively show that the gas is outflowing. In both SPT 2354−58 and 0314−44, the emission components are far redshifted, which is consistent with outflowing gas in

[4] Although the sources are substantially more compact than the beam sizes, residual phase errors may result in finite fitted sizes, such that peak fluxes would underestimate the total fluxes. As such, it is best practice to extract fluxes from size fits if the signal-to-noise ratio of the detection is sufficiently high, as is the case for all continuum detections reported here.

[5] Line fluxes were extracted from the moment-0 maps in the same way as continuum fluxes when the signal-to-noise ratio was sufficient, and then compared to peak fluxes to evaluate whether or not a line is resolved in the data and thus requires an aperture correction to its peak flux spectrum as extracted from the brightest pixel in the moment-0 map. For lines too faint to provide reliable size fits, aperture corrections were adopted from the brightest emission line for emission lines, and from the continuum for absorption lines, but the center of the aperture was placed on the peak pixel of the faint line in its moment-0 map. This is to allow for small spatial offsets, e.g., between the absorption and emission components of lines with P-Cygni profiles. For reference, the average aperture correction in Figure 2 is 13.3%, with a factor of ~2 scatter toward the most extreme values.

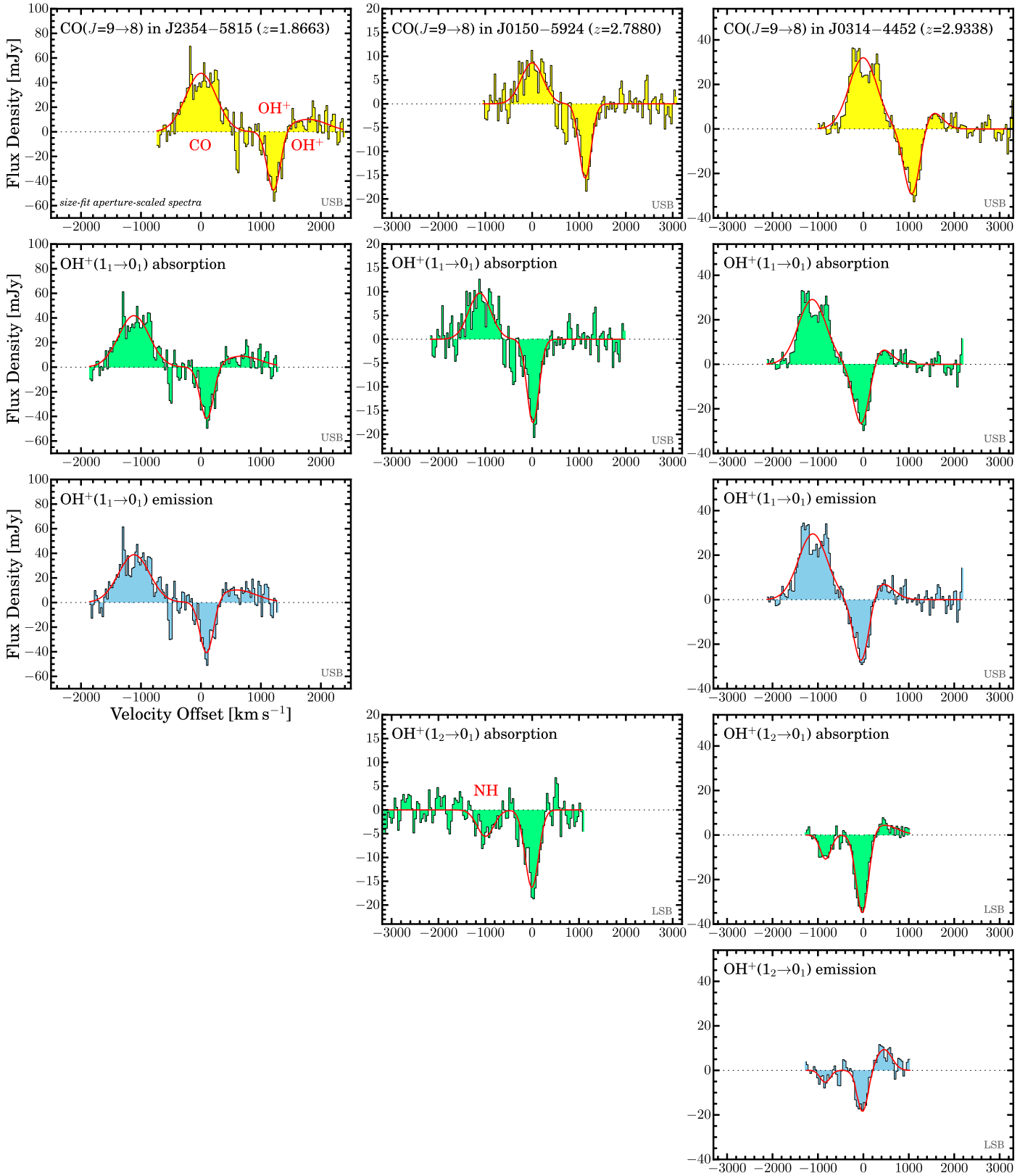

Figure 2. Line spectra toward SPT 2354−58, 0150−59, and 0314−44 at a spectral resolution of 31.25 MHz (histograms) and multicomponent Gaussian fits to all features (red lines; left to right). Spectra are extracted from apertures scaled to the fitted size in the moment-0 map of the main line indicated in each panel after continuum subtraction, and scaled to the CO($J = 9 \rightarrow 8$) systemic redshifts. Peak spectra are used where the size fits are most consistent with a point source. All features are fitted simultaneously, but only the parameters for the main features are adopted (no separate plots are shown for NH).

Table 3
Line Properties of the "Confirmed" Sources

	SPT 2354−58	SPT 0150−59	SPT 0314−44
z_{CO}	1.8663 ± 0.0002	2.7880 ± 0.0004	2.9338 ± 0.0002
$I_{CO(9-8)}$ (Jy km s^{-1})	30.2 ± 1.9	5.05 ± 0.59	24.6 ± 1.2
dv_{FWHM} (km s^{-1})	600 ± 40	550 ± 70	730 ± 40
$L'_{CO(9-8)}$ (10^{10} L_l)[a]	6.72 ± 0.42	2.27 ± 0.27	12.04 ± 0.59
$L_{CO(9-8)}$ (10^8 $L_\odot$)[a]	24.0 ± 1.5	8.09 ± 0.95	42.9 ± 2.1
$I_{H2O(202-111)}$ (Jy km s^{-1})	...	...	18.4 ± 1.5
dv_{FWHM} (km s^{-1})	...	...	795 ± 75
$v_0 - v_{0,CO}$ (km s^{-1})	...	...	−28 ± 29
L'_{H2O} (10^{10} L_l)[a]	...	...	9.9 ± 0.8
L_{H2O} (10^8 $L_\odot$)[a]	...	...	30.6 ± 2.5
$I^{abs}_{OH+(11-01)}$ (Jy km s^{-1})	−12.2 ± 2.8	−5.6 ± 0.9	−12.3 ± 4.3
dv_{FWHM} (km s^{-1})	260 ± 40	300 ± 30	420 ± 70
$v_0 - v_{0,CO}$ (km s^{-1})	100 ± 13	18 ± 13	−40 ± 50
τ_{OH+}	$0.86^{+0.38}_{-0.27}$	$0.42^{+0.09}_{-0.08}$	$0.42^{+0.20}_{-0.08}$
$\tau_{OH+}dv$ (km s^{-1})	380^{+170}_{-120}	271^{+57}_{-52}	300^{+140}_{-55}
$N(OH^+)$ (10^{14} cm^{-2})[b]	$18.5^{+8.3}_{-5.8}$	$13.2^{+2.8}_{-2.5}$	$14.6^{+6.8}_{-2.7}$
N(H) (10^{22} cm^{-2})[b]	$11.7^{+5.2}_{-3.7}$	$8.3^{+1.7}_{-1.6}$	$9.2^{+4.3}_{-1.7}$
$I^{abs}_{OH+(12-01)}$ (Jy km s^{-1})	...	−5.8 ± 0.9	−12.4 ± 1.8
dv_{FWHM} (km s^{-1})	...	330 ± 30	320 ± 20
$v_0 - v_{0,CO}$ (km s^{-1})	...	−6 ± 13	−20 ± 7
τ_{OH+}	...	$0.50^{+0.12}_{-0.11}$	$0.57^{+0.29}_{-0.11}$
$\tau_{OH+}dv$ (km s^{-1})	...	274^{+65}_{-58}	320^{+160}_{-60}
$I^{em}_{OH+(11-01)}$ (Jy km s^{-1})	8.6 ± 4.1	...	4.8 ± 3.2
dv_{FWHM} (km s^{-1})	800 ± 500	...	600 ± 500
$v_0 - v_{0,CO}$ (km s^{-1})	600 ± 200	...	<400 ± 300
$L'_{OH+(1-0)}$ (10^{10} L_l)[a]	1.93 ± 0.92	...	2.4 ± 1.6
$L_{OH+(1-0)}$ (10^8 $L_\odot$)[a]	6.8 ± 3.2	...	8.4 ± 5.6
$I^{em}_{OH+(12-01)}$ (Jy km s^{-1})	...	...	4.0 ± 1.4
dv_{FWHM} (km s^{-1})	...	...	400 ± 90
$v_0 - v_{0,CO}$ (km s^{-1})	...	...	460 ± 40
$L'_{OH+(1-0)}$ (10^{10} L_l)[a]	...	...	2.2 ± 0.8
$L_{OH+(1-0)}$ (10^8 $L_\odot$)[a]	...	...	6.5 ± 2.3
$I^{abs}_{NH(12-01)}$ (Jy km s^{-1})	...	−1.91 ± 0.75	−3.57 ± 0.76
dv_{FWHM} (km s^{-1})	...	420 ± 100	280 ± 40
$v_0 - v_{0,CO}$ (km s^{-1})	...	−170 ± 40	−6 ± 15
τ_{NH}	...	$0.20^{+0.09}_{-0.08}$	$0.19^{+0.04}_{-0.04}$
$\tau_{NH}dv$ (km s^{-1})	...	122^{+56}_{-51}	71^{+17}_{-16}

Notes.
[a] Given in units of L_l = K km s^{-1} pc^2. Luminosities are "apparent," i.e., not corrected for gravitational magnification (μ_L = 6.3 ± 0.4 for SPT 2354−58; J. S. Spilker et al. 2016; unknown for the other sources).
[b] See N. Indriolo et al. (2018), S. Bialy et al. (2019), and D. A. Riechers et al. (2021a) for conversions from optical depth to column densities N of OH^+ and atomic hydrogen.

these two sources.[6] Lastly, we also detect $H_2O(J_{K_aK_c}=2_{02}\rightarrow 1_{11})$ emission at 15σ peak significance toward SPT 0314−44 (Figure 3). This unambiguously confirms the redshifts of all sources. Line parameters were obtained from Gaussian fitting to the line profiles, using multiple Gaussian components where appropriate. From the CO($J=9\rightarrow 8$) lines, we measure systemic $z_{CO}=1.8663\pm0.0002$, 2.7880 ± 0.0004, and 2.9338 ± 0.0002, respectively. All line parameters are summarized in Table 3. These observations will be analyzed further in concert with the full sample of ~70 sources observed in the same program (D. Riechers et al. 2025, in preparation).[7]

3.2. Revised Redshift

We successfully detect continuum emission in the Band 5, 6, and 7 observations of SPT 0452−50 presented here for the first

[6] While differential lensing between different gas components could partially explain differences in line shapes between different species, we expect these effects to be subdominant to real differences in the velocities of different gas components. While a broader analysis is beyond the scope of this work, these considerations are supported by the analysis of high-resolution CO and OH^+ observations of other, similarly bright DSFGs (e.g., S. Berta et al. 2021; K. M. Butler et al. 2021).

[7] In parallel to this work, G. Gururajan et al. (2023) have also independently confirmed the redshifts of SPT 2354−58 and 0150−59 based on CO($J=7\rightarrow 6$) and [C I] detections.

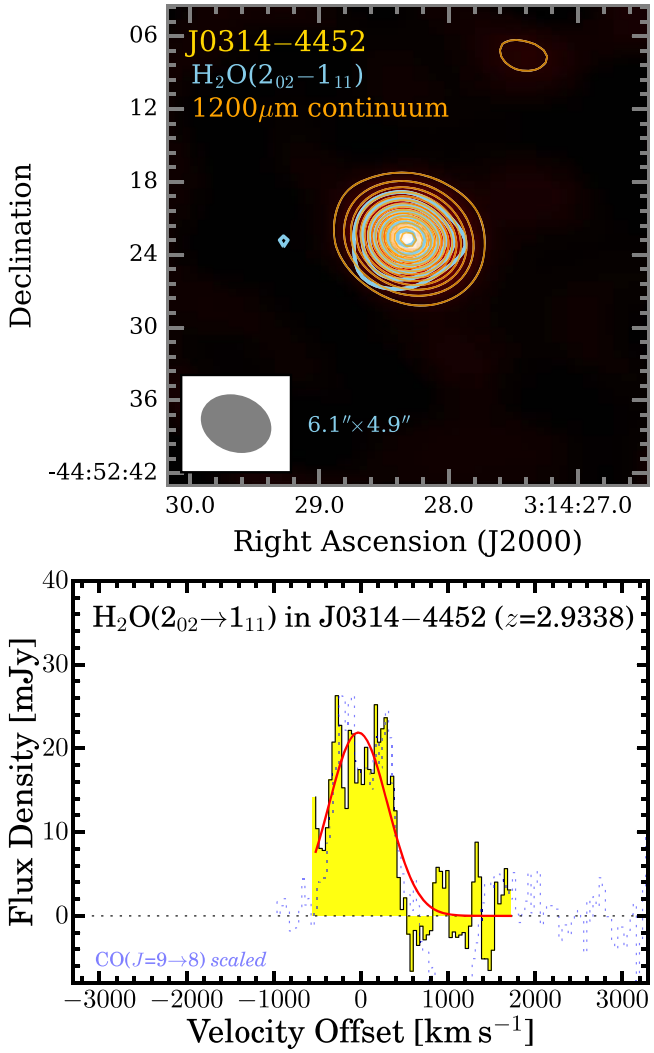

Figure 3. $H_2O(2_{02} \rightarrow 1_{11})$ map (top) and spectrum (bottom) toward SPT 0314 −44, in the same style as in Figures 1 and 2. For comparison, a scaled version of the CO($J = 9 \rightarrow 8$) spectrum is shown as a dotted histogram (bottom).

time (Figure 4). The peak significance of the detections ranges between 34 and 70σ (Table 2) and remains virtually unresolved, as is expected based on its compact size seen at higher spatial resolution (Figure 4, top left).

We however do not detect the targeted CO($J = 9 \rightarrow 8$) and $OH^+(N_J = 1_1 \rightarrow 0_1)$ lines at $z = 2.011$. Instead, the data show a single emission line detected at 9.0σ peak significance at an unexpected frequency (Figure 5). This line would be consistent with the expected redshifted frequency of [O I] 146 μm if the two CO lines reported by M. Aravena et al. (2016) and A. Weiß et al. (2013) were to be due to CO($J = 2 \rightarrow 1$) and CO($J = 6 \rightarrow 5$) emission at $z = 5.016$, instead of CO($J = 1 \rightarrow 0$) and CO($J = 3 \rightarrow 2$) emission at $z = 2.011$ as previously reported. However, this redshift was seemingly ruled out due to the nondetection of CO($J = 5 \rightarrow 4$) in the 3 mm line scan reported by A. Weiß et al. (2013).

To further investigate this issue, we analyzed archival data targeting both [C I] lines in this source at $z = 2.011$. No [C I] or CO lines are detected in these observations, but they show weak evidence for a H_2O $2_{02} \rightarrow 1_{11}$ line at 4.8σ significance at a frequency consistent with $z = 5.016$. We then reanalyzed the 3 mm line scan data reported by A. Weiß et al. (2013). These data show weak evidence for a CO($J = 5 \rightarrow 4$) line at 5.1σ significance at a frequency consistent with $z = 5.016$. We speculate that this line may have been missed due to the conservative edge channel flagging applied by the standard ALMA calibration procedures, but we cannot confirm this based on the archived data products. This line, however, is much weaker than the CO($J = 3 \rightarrow 2$) line reported by the same authors (which, in this scenario, would be CO $J = 6 \rightarrow 5$), resulting in unrealistically high line brightness temperature ratios.

Given the reliance on weak line features and unusual circumstances, we targeted the [C II] line at $z = 5.016$ to break the degeneracy between the different scenarios. We detect [C II] emission at 29σ peak significance, which unambiguously determines the redshift to be $z_{\rm C\ II} = 5.0160 \pm 0.0005$ (Figure 4). This implies that the line detected by M. Aravena et al. (2016) is CO($J = 2 \rightarrow 1$) instead of CO($J = 1 \rightarrow 0$), and the line detected by A. Weiß et al. (2013), if confirmed, is CO($J = 6 \rightarrow 5$) instead of CO($J = 3 \rightarrow 2$).

Upon closer inspection, we also find evidence for three weak absorption features due to $OH^+(N_J = 1_1 \rightarrow 0_1)$, $NH(N_J = 2_2 \rightarrow 1_2)$, and $CH(N_J = 2_{-1} \rightarrow 1_1)$ at 4.0, 4.3, and 3.4σ peak significance. OH^+ also shows evidence for a redshifted emission component, but only at 2.5σ peak significance. Together with the blueshift of the absorption component, this suggests the presence of outflowing gas. NH and CH are only partially covered by the bandpass, such that their line optical depths remain uncertain. All line parameters are summarized in Table 4.

4. Analysis and Discussion

4.1. SED Modeling

Motivated by the added dust photometry for the first three sources and the revised redshift and additional data for the fourth source, we have refit their SEDs based on modified blackbody (MBB) models to their rest-frame far-infrared to millimeter wavelength emission. As described in more detail in our previous works (e.g., D. A. Riechers et al. 2013; C. D. Dowell et al. 2014), we use a Markov Chain Monte Carlo–based approach for this purpose. The procedure, called `MBB_EMCEE`, uses the dust temperature $T_{\rm dust}$, the spectral slope of the dust emissivity $\beta_{\rm IR}$, and the wavelength λ_0 where the dust optical depth reaches unity as the main fit parameters. To approximately capture the falloff of the SEDs on the far Wien side, we join the MBB to a power law with the shape $\propto\nu^{\alpha}$ on the short-wavelength side of its peak. All fits are normalized to the observed-frame 500 μm continuum flux of each source. As done in our previous work, we place a broad prior of $\beta_{\rm IR} = 1.8 \pm 0.6$ on the dust emissivity parameter to guide the fitting. This choice is motivated by the $\beta_{\rm IR}$ found for molecular clouds in the Milky Way (e.g., Planck Collaboration et al. 2011).

We have also refit the dust SEDs of all known $z > 5$ DSFGs with the same procedure, except in those cases where this had already been done in the literature (D. A. Riechers et al. 2020, 2021a, 2021b). The main motivation for this step were the significant changes in parameters reported for the SPT sample between the procedures used by M. L. Strandet et al. (2016) and C. Reuter et al. (2020). While different approaches to the fitting are valid, we decided to restrict our comparison to samples fit with our procedure in order to minimize potential biases in the comparison. That being said, the differences between parameters reported by us and C. Reuter et al. (2020)

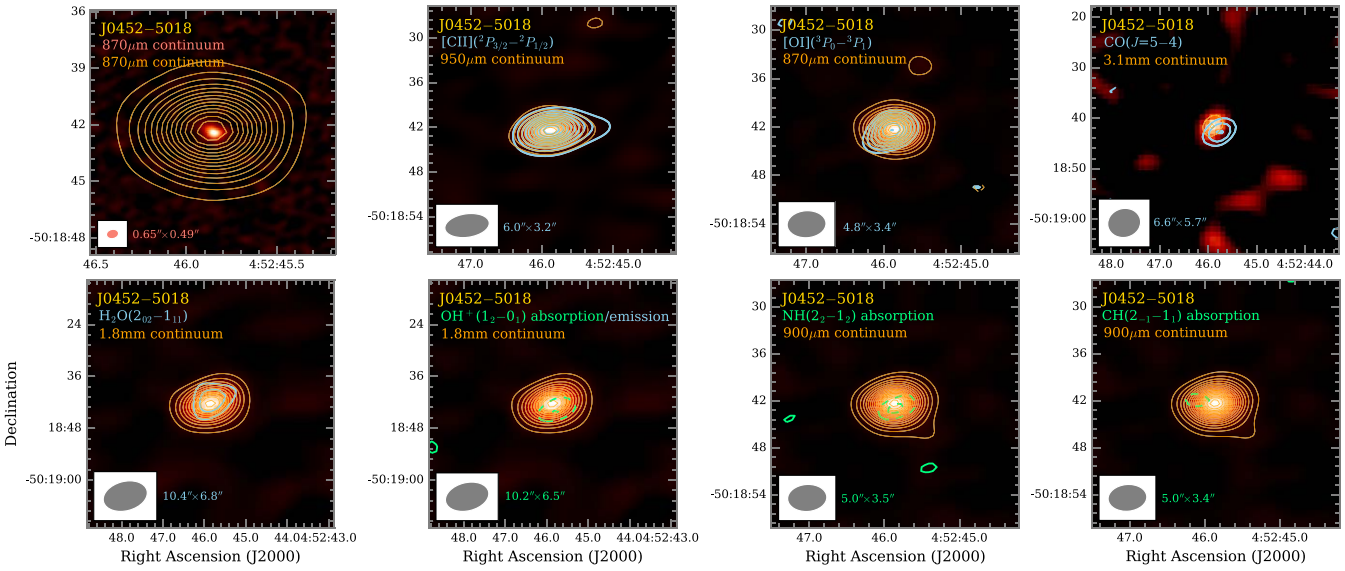

Figure 4. Line and continuum emission toward SPT 0452−50. Top left: USB continuum contours from the [O I] observations, overlaid on an archival ALMA 870 μm high-resolution continuum image (project ID: 2011.0.00958.S; background data previously published by J. S. Spilker et al. 2016). Remainder top row, left to right: [C II] 158 μm, [O I] 146 μm, and CO($J = 5 \rightarrow 4$) contours overlaid on the continuum emission at the same wavelengths, in the same style as Figure 1. Bottom row, left to right: $H_2O(2_{02} \rightarrow 1_{11})$ emission contours and $OH^+(N_J = 1_1 \rightarrow 0_1)$, NH($N_J = 2_2 \rightarrow 1_2$), and CH($N_J = 2_{-1} \rightarrow 1_1$) absorption contours overlaid on the continuum emission at the same wavelengths. Continuum contours in the second to eighth panels are shown in steps of $\pm 3\sigma$, where $1\sigma = 0.98$, 0.97, 0.17, 0.18, 0.18, 0.84, and 0.84 mJy beam^{-1} (except for CO $J = 5 \rightarrow 4$, where contours start at $\pm 3\sigma$ and are shown in steps of 1σ), respectively. Line contours are shown in steps of 1σ, starting at $\pm 3\sigma$, except for [C II], where contours are shown in steps of 3σ. In the same order, $1\sigma = 1.9$, 1.6, 0.69, 0.42, 0.68, 3.6, and 3.6 mJy beam^{-1}, respectively. OH^+ emission contours ($1\sigma = 0.89$ mJy beam^{-1}) are also included but do not appear because the signal is $<3\sigma$ significant.

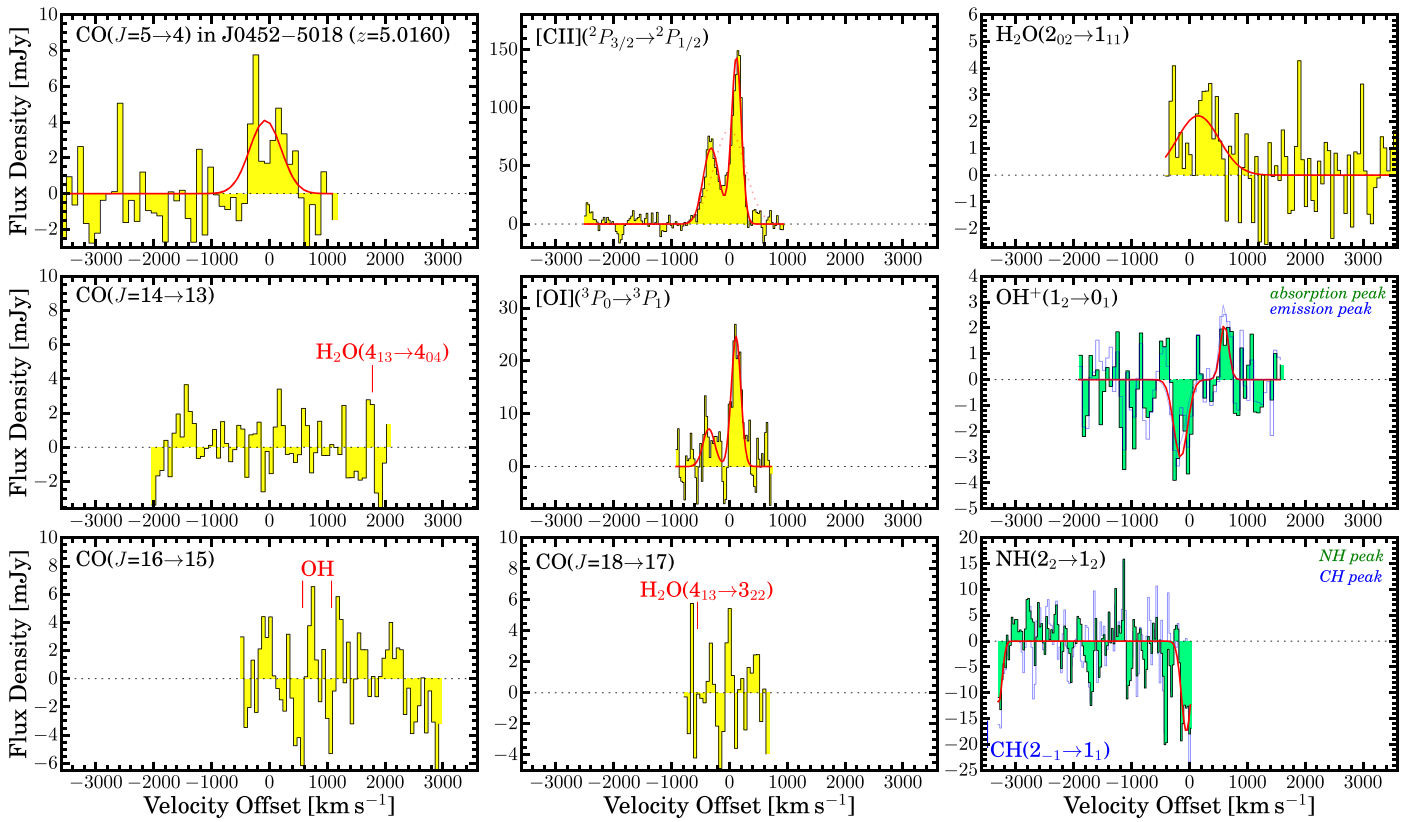

Figure 5. Line spectra toward SPT 0452−50 at a spectral resolution of 31.25 MHz (histograms; except CO upper-limit spectra, which are shown at half the resolution) and multicomponent Gaussian fits to all features, in the same style as Figure 2. Spectra are scaled to the [C II] flux-weighted systemic redshift (center velocity of single-Gaussian fit; dotted curve). Red/blue markers indicate the center velocities of additional features. The OH^+ emission and CH absorption peaks are tentative and require independent confirmation. Fit parameters to the NH/CH spectra are unreliable due to the incomplete line coverage, and thus are discarded in the analysis.

Table 4
Line Properties of SPT 0452−50

Line	$I_{\rm line}$ (Jy km s^{-1})	$dv_{\rm FWHM}$ (km s^{-1})	$v_0 - v_{0,\rm C\,II}$ (km s^{-1})	$L'_{\rm line}$[a] (10^{10} L_l)	$L_{\rm line}$[a] (10^8 $L_\odot$)	$\tau_{\rm line}$	$\tau_{\rm line}dv$ (km s^{-1})
CO(J = 2 → 1)[b]	0.96 ± 0.12	610 ± 60	⋯	22.3 ± 2.8	0.88 ± 0.11	⋯	⋯
CO(J = 5 → 4)	2.80 ± 0.67	640 ± 180	−70 ± 75	10.4 ± 2.5	6.4 ± 1.5	⋯	⋯
CO(J = 14 → 13)	<1.3	(630)	⋯	<0.64	<8.5	⋯	⋯
CO(J = 16 → 15)	<2.7	(630)	⋯	<1.0	<20	⋯	⋯
CO(J = 18 → 17)	<2.0	(630)	⋯	<0.57	<16	⋯	⋯
$H_2O(J_{K_aK_c} = 2_{02} \rightarrow 1_{11})$	2.02 ± 0.52	860 ± 260	150 ± 100	2.56 ± 0.66	7.9 ± 2.0	⋯	⋯
$H_2O(J_{K_aK_c} = 4_{13} \rightarrow 3_{22})$	<1.4	(630)	⋯	<0.41	<12	⋯	⋯
$H_2O(J_{K_aK_c} = 4_{13} \rightarrow 4_{04})$	<1.5	(630)	⋯	<0.73	<9.6	⋯	⋯
OH($^2\Pi_{1/2}$ J = 3/2 → 1/2)	<4.1	*(1130)*	⋯	<1.5	<30	⋯	⋯
$OH^+(N_J = 1_2 \rightarrow 0_1)$ abs.	−0.89 ± 0.47	280 ± 90	−150 ± 40	⋯	⋯	$0.82^{+1.10}_{-0.51}$	300^{+410}_{-190}
$OH^+(N_J = 1_2 \rightarrow 0_1)$ em.	*0.5 ± 0.2*	*160 ± 60*	*595 ± 25*	*0.65 ± 0.26*	*1.9 ± 0.8*		
$NH(N_J = 2_2 \rightarrow 1_2)$	~(−2.94 ± 0.72)	(200)	⋯	⋯	⋯	$\sim(0.50^{+0.17}_{-0.15})$	$>(100^{+35}_{-30})$
$CH(N_J = 2_{-1} \rightarrow 1_1)$	*<(−1.78 ± 0.51)*	*(140)*	⋯	⋯	⋯	$0.93^{+0.58}_{-0.36}$	$>(130^{+80}_{-50})$
[C II]($^2P_{3/2} \rightarrow {}^2P_{1/2}$)	54.8 ± 4.0	630 ± 50	0	18.8 ± 1.4	410 ± 30	⋯	⋯
[O I]($^3P_0 \rightarrow {}^3P_1$)	7.4 ± 1.3	600 ± 120	90 ± 50	2.15 ± 0.38	60 ± 11	⋯	⋯

Notes. All quoted upper limits are 3σ.
[a] Given in units of L_l = K km s^{-1} pc^2. Luminosities are "apparent," i.e., not corrected for gravitational magnification ($\mu_{\rm L}$=1.7 ± 0.1; J. S. Spilker et al. 2016).
[b] Line flux and width adopted from M. Aravena et al. (2016).

Table 5
SED Parameters for the Target Sample

	SPT 2354 −58	SPT 0150 −59	SPT 0314 −44	SPT 0452 −50
$T_{\rm dust}$ (K)	$69.2^{+0.8}_{-1.2}$	$45.9^{+4.3}_{-8.5}$	$54.9^{+0.4}_{-2.3}$	$76.2^{+2.5}_{-2.5}$
$\beta_{\rm IR}$	$2.18^{+0.03}_{-0.09}$	$1.73^{+0.02}_{-0.09}$	$2.44^{+0.01}_{-0.10}$	$2.30^{+0.13}_{-0.13}$
$\lambda_{\rm peak}$ (μm)	74^{+1}_{-1}	86^{+3}_{-1}	93^{+3}_{-1}	67^{+2}_{-2}
λ_0 (μm)	232^{+4}_{-9}	108^{+37}_{-61}	233^{+2}_{-16}	229^{+9}_{-9}
$L_{\rm FIR}$ (10^{13} $L_\odot$)[a]	$5.82^{+0.11}_{-0.08}$	$3.25^{+0.13}_{-0.19}$	$7.44^{+0.19}_{-0.15}$	$4.01^{+0.15}_{-0.14}$
$L_{\rm IR}$ (10^{13} $L_\odot$)[a]	$9.40^{+0.22}_{-0.33}$	$5.00^{+0.09}_{-0.99}$	$10.76^{+0.27}_{-0.35}$	$6.96^{+0.42}_{-0.46}$

Note.
[a] Apparent values not corrected for gravitational magnification ($\mu_{\rm L}$ = 6.3 ± 0.4 and 1.7 ± 0.1 for SPT 2354–58 and 0452–50, respectively; J. S. Spilker et al. 2016). $L_{\rm FIR}$ ($L_{\rm IR}$) is integrated over 42.5–122.5 μm (8–1000 μm) in the rest frame.

for the same sources are mostly minor, and can perhaps be explained by the inclusion of additional photometry in our fits. The results for the galaxies analyzed in detail in this work are summarized in Table 5, and those for the entire $z > 5$ DSFG sample are summarized in Table 6. The corresponding data and fits are shown in Figure 6.

4.2. SPT 0452−50 As a z > 5 DSFG

4.2.1. Physical Properties from Molecular Line Strengths

As a proxy for the gas excitation, we can investigate the CO(J = 5 → 4) to CO(J = 2 → 1) line brightness temperature ratio r_{52} of SPT 0452−50. Given the impact of the warmer CMB at higher redshift, direct comparisons only make sense to sources at similar redshifts. For SPT 0452−50, we find r_{52}=0.47 ± 0.11. For the three z = 5.2–5.3 DSFGs HDF 850.1, AzTEC-3, and GN10, D. A. Riechers et al. (2020) have found r_{52} = 0.54 ± 0.11, 0.78 ± 0.07, and 0.47 ± 0.11, respectively. For the z = 5.2 DSFG HLS 0918, one can find r_{52} = 0.41 ± 0.03 based on the fluxes reported by T. D. Rawle et al. (2014). For the z = 5.7 DSFG ADFS-27, D. A. Riechers et al. (2021b) have found r_{52} = 0.60 ± 0.05. For the z = 5.7 DSFG CRLE, D. Vieira et al. (2022) have found r_{52} = 0.71 ± 0.07. The median (average) for this sample is r_{52} = 0.54 ± 0.07 (r_{52} = 0.57 ± 0.14), where the uncertainties are the median absolute deviation and the standard deviation, respectively. As such, the r_{52} of SPT 0452−50 appears to be indicative of a rather "typical" CO excitation for a $z > 5$ DSFG. This finding may call the previously found strength (spectra shown by A. Weiß et al. 2013 and C. Reuter et al. 2020) of the line now identified as CO(J = 6 → 5) into question, but since no flux was reported for this line previously, we cannot conclusively investigate this issue further.

C. Yang et al. (2016) have presented a relation between the $H_2O(J_{K_aK_c} = 2_{02} \rightarrow 1_{11})$ line luminosity and $L_{\rm IR}$, with a near-linear power-law slope of 1.06 ± 0.19. SPT 0452–50 follows this relation, which is consistent with a picture in which infrared pumping contributes substantially to the excitation of the rotational H_2O lines (see also, e.g., E. González-Alfonso et al. 2012; D. A. Riechers et al. 2013). Its H_2O properties thus appear typical for a massive DSFG.

From the CO(J = 2 → 1) luminosity of SPT 0452−50 at its revised redshift of z = 5.016, we find a lensing-corrected total molecular gas mass of $M_{\rm gas}(\alpha_{\rm CO}) = 1.3 \times 10^{11}\,M_\odot$, where $\alpha_{\rm CO} = 1.0\,M_\odot$ (K km s^{-1} pc^2)$^{-1}$ is the adopted conversion factor from CO luminosity to gas mass (e.g., D. A. Riechers et al. 2013). We here neglected the excitation correction from CO(J = 2 → 1) to CO(J = 1 → 0), as we consider it minor compared to other sources of uncertainty. From $L_{\rm IR}$, we find a dust-obscured massive star formation rate of $\rm SFR_{IR} = 4100\,M_\odot\,yr^{-1}$. This yields a gas depletion time of $M_{\rm gas}/\rm SFR_{IR}$ = 32 Myr, which is rather typical for a massive DSFG.

4.2.2. [C II]/[O I] Luminosity Ratio

The ratio between the fraction of [C II] to emerge from the neutral interstellar medium and [O I] is an indicator of the density of photon-dominated regions (PDRs; e.g., M. L. Luhman et al. 2003). We find a luminosity ratio of $r_{\rm CII,OI}$ = 6.8 ± 1.3 for SPT 0452–50. For the z = 5.3 and 5.7 DSFGs AzTEC-3 and

Table 6
SED Parameters for All Known $z > 5$ DSFGs

Name	z	μ_L[a]	T_{dust} (K)	β_{IR}	λ_{peak} (μm)	λ_0 (μm)	L_{FIR}^{b} (10^{13} $L_\odot$)	L_{IR}^{b} (10^{13} $L_\odot$)
SPT 0452−50	5.0160	1.7 ± 0.1	$76.2^{+2.5}_{-2.5}$	$2.30^{+0.13}_{-0.13}$	67^{+2}_{-2}	229^{+9}_{-9}	$4.01^{+0.15}_{-0.14}$	$6.96^{+0.42}_{-0.46}$
SPT 0202−61	5.0182	8.3 ± 1.0	$79.1^{+2.5}_{-2.6}$	$2.74^{+0.23}_{-0.21}$	64^{+2}_{-2}	297^{+17}_{-15}	$8.04^{+0.25}_{-0.21}$	$15.11^{+0.90}_{-0.84}$
HXMM-30	5.0940	*s*	$74.2^{+4.7}_{-4.6}$	$2.64^{+0.37}_{-0.39}$	69^{+4}_{-4}	242^{+29}_{-34}	$2.47^{+0.18}_{-0.17}$	$4.41^{+0.42}_{-0.64}$
SPT 0425−40	5.1353	*s*	$75.7^{+1.9}_{-5.7}$	$2.72^{+0.44}_{-0.39}$	68^{+4}_{-3}	211^{+29}_{-41}	$6.11^{+0.30}_{-0.20}$	$10.62^{+0.40}_{-0.86}$
HeLMS-34	5.1614	*s*	$63.0^{+7.8}_{-8.3}$	$1.36^{+0.14}_{-0.18}$	66^{+2}_{-2}	93^{+50}_{-64}	$5.38^{+0.21}_{-0.20}$	$8.65^{+0.51}_{-0.78}$
HDF 850.1	5.1833	1.6 ± 0.3	$51.6^{+15.6}_{-15.1}$	$2.67^{+0.30}_{-0.30}$	85^{+13}_{-13}	136^{+45}_{-49}	$0.52^{+0.17}_{-0.18}$	$0.74^{+0.30}_{-0.29}$
SPT 2203−41	5.1937	*s*	$54.0^{+6.1}_{-6.0}$	$3.16^{+0.34}_{-0.32}$	94^{+9}_{-9}	219^{+27}_{-31}	$3.48^{+0.21}_{-0.19}$	$8.52^{+2.16}_{-3.04}$
SXDF 1100.053	5.2383	⋯	$61.6^{+19.0}_{-20.7}$	$2.58^{+0.26}_{-0.26}$	83^{+20}_{-20}	208^{+40}_{-69}	$0.40^{+0.15}_{-0.17}$	$0.62^{+0.31}_{-0.32}$
HLS 0918	5.2430	8.9 ± 1.9	$64.9^{+2.5}_{-3.2}$	$2.69^{+0.30}_{-0.26}$	78^{+3}_{-3}	196^{+4}_{-31}	$10.26^{+0.59}_{-0.41}$	$15.95^{+0.64}_{-1.07}$
HLock-102	5.2915	12.5 ± 1.2	$55.7^{+5.1}_{-7.5}$	$1.80^{+0.07}_{-0.08}$	73^{+2}_{-1}	99^{+31}_{-43}	$6.82^{+0.15}_{-0.13}$	$9.67^{+0.34}_{-0.50}$
SPT 2319−55	5.2927	7.9 ± 1.9	$68.6^{+4.0}_{-4.8}$	$2.72^{+0.35}_{-0.31}$	75^{+5}_{-5}	234^{+23}_{-29}	$2.78^{+0.21}_{-0.19}$	$4.62^{+0.43}_{-0.57}$
AzTEC-3	5.2980	⋯	$92.5^{+15.4}_{-15.9}$	$2.09^{+0.21}_{-0.21}$	55^{+8}_{-8}	181^{+33}_{-34}	$1.12^{+0.16}_{-0.16}$	$2.55^{+0.73}_{-0.74}$
GN10	5.3031	⋯	$48.8^{+9.0}_{-11.2}$	$3.18^{+0.26}_{-0.21}$	96^{+9}_{-9}	170^{+20}_{-36}	$0.64^{+0.11}_{-0.12}$	$1.18^{+0.19}_{-0.21}$
SPT 0553−50	5.3201	*s*	$57.8^{+7.1}_{-8.8}$	$2.00^{+0.21}_{-0.19}$	79^{+5}_{-4}	158^{+44}_{-55}	$3.13^{+0.26}_{-0.23}$	$4.69^{+0.46}_{-0.60}$
HELMS45	5.3994	*s*	$92.9^{+4.7}_{-4.7}$	$2.19^{+0.31}_{-0.32}$	55^{+3}_{-2}	187^{+23}_{-22}	$7.19^{+0.26}_{-0.25}$	$16.3^{+0.64}_{-1.81}$
SPT 2353−50	5.5781	s_c	$72.0^{+4.6}_{-5.5}$	$2.53^{+0.35}_{-0.32}$	71^{+5}_{-4}	220^{+26}_{-34}	$3.28^{+0.24}_{-0.21}$	$5.62^{+0.54}_{-0.70}$
SPT 0245−63	5.6256	⋯	$55.7^{+6.6}_{-18.5}$	$2.38^{+0.21}_{-0.19}$	88^{+12}_{-7}	179^{+36}_{-64}	$3.78^{+0.26}_{-0.25}$	$18.2^{+1.42}_{-1.26}$
SPT 0348−62	5.6541	1.18 ± 0.01	$64.4^{+3.6}_{-5.2}$	$2.65^{+0.28}_{-0.21}$	79^{+5}_{-4}	197^{+17}_{-29}	$3.36^{+0.26}_{-0.21}$	$5.35^{+0.49}_{-0.64}$
ADFS-27	5.6550	⋯	$59.2^{+3.3}_{-4.1}$	$2.52^{+0.19}_{-0.17}$	85^{+5}_{-4}	191^{+11}_{-19}	$1.58^{+0.10}_{-0.19}$	$2.38^{+0.23}_{-0.22}$
SPT 0346−52	5.6554	5.6 ± 0.1	$75.9^{+1.9}_{-2.2}$	$2.37^{+0.22}_{-0.23}$	67^{+2}_{-2}	195^{+12}_{-14}	$12.01^{+0.34}_{-0.27}$	$20.41^{+0.65}_{-0.67}$
CRLE	5.6666	1.09 ± 0.02	$62.6^{+3.9}_{-3.5}$	$1.61^{+0.44}_{-0.45}$	76^{+2}_{-2}	180^{+39}_{-44}	$1.61^{+0.06}_{-0.06}$	$2.62^{+0.40}_{-0.25}$
SPT 0243−49	5.7022	5.1 ± 0.5	$41.9^{+10.0}_{-10.8}$	$2.16^{+0.24}_{-0.24}$	101^{+6}_{-6}	155^{+64}_{-73}	$3.66^{+0.27}_{-0.27}$	$7.59^{+1.82}_{-2.03}$
SPT 2351−57	5.8114	s_c	$85.6^{+4.1}_{-5.0}$	$2.90^{+0.53}_{-0.57}$	60^{+3}_{-3}	232^{+28}_{-39}	$3.92^{+0.23}_{-0.18}$	$7.74^{+0.61}_{-0.70}$
ID 85001929	5.847	⋯	$59.0^{+7.7}_{-16.7}$	$2.49^{+0.04}_{-0.38}$	68^{+5}_{-2}	117^{+11}_{-72}	$0.58^{+0.08}_{-0.07}$	$0.87^{+0.10}_{-0.14}$
HeLMS-54ab	5.880	⋯	⋯	⋯	⋯	⋯	⋯	⋯
G09-83808	6.0269	8.2 ± 0.3	$57.4^{+8.7}_{-8.9}$	$2.65^{+0.34}_{-0.33}$	83^{+6}_{-6}	174^{+49}_{-47}	$2.44^{+0.33}_{-0.32}$	$3.61^{+0.52}_{-0.58}$
J1353−0010	6.1694	⋯	$75.1^{+21.6}_{-21.7}$	$1.90^{+0.52}_{-0.53}$	60^{+11}_{-11}	109^{+43}_{-64}	$0.69^{+0.13}_{-0.13}$	$1.39^{+0.55}_{-0.59}$
HFLS3	6.3369	1.8 ± 0.6	$63.3^{+5.4}_{-5.8}$	$1.94^{+0.07}_{-0.09}$	73^{+2}_{-1}	142^{+25}_{-27}	$2.93^{+0.14}_{-0.13}$	$5.50^{+0.30}_{-0.22}$
SPT 0311−58	6.9011	2.0 ± 0.2	$80.4^{+8.4}_{-8.3}$	$2.51^{+0.41}_{-0.40}$	64^{+6}_{-6}	213^{+33}_{-35}	$3.97^{+0.40}_{-0.37}$	$8.32^{+0.94}_{-1.71}$
Median	5.36 ± 0.27	⋯	63.9 ± 9.0	2.52 ± 0.21	73 ± 8	189 ± 31	⋯	⋯
Average	5.52 ± 0.44	⋯	66.6 ± 12.7	2.41 ± 0.43	74 ± 12	185 ± 47	⋯	⋯

Notes. Photometry, redshifts, and μ_L used in the analysis are adopted from this work and C. Reuter et al. (2020) for all SPT sources; S. Ikarashi et al. (2022) for SXDF1100.053 (a.k.a. ASXDF1100.053.1); D. A. Riechers et al. (2021b) for ADFS-27; D. A. Riechers et al. (2021a) for HXMM-30, HeLMS-34, and HLock-102; P. Cox et al. (2023) for HELMS45; this work for J1353−0010; and D. A. Riechers et al. (2020) for the remainder of the sample. The latter compilation includes additional data from T. D. Rawle et al. (2014), D. A. Riechers et al. (2010, 2013, 2014, 2017), R. Pavesi et al. (2018), S. Jin et al. (2019), Y. Fudamoto et al. (2017), and J. A. Zavala et al. (2018). Fluxes used for J1353−0010 at (3.4, 4.6, 12.1, 22.2, 635, 651, 1132, and 1195) μm are (<0.0261, <0.0187, <0.0756, <5.28, 8.5 ± 1.2, 8.09 ± 0.42, 3.00 ± 0.18, and 2.19 ± 0.11) mJy, respectively, based on archival Wide-field Infrared Survey Explorer and ALMA data. The near-infrared fluxes reported by I. Mitsuhashi et al. (2024) are only used as upper-limit constraints to the Wien side for the dust SED. Other sources reported by these authors are too faint to make the luminosity cut of the sample considered here.

[a] Lensing magnification factor. Source thought to be strongly lensed but with unknown magnification factors (unlensed) are indicated with an "s" (empty column). An index "c" indicates that the source was identified as a cluster-lensed system by J. S. Spilker et al. (2016).

[b] Apparent values not corrected for gravitational magnification. L_{FIR} (L_{IR}) is integrated over 42.5–122.5 μm (8–1000 μm) in the rest frame.

CRLE, R. Pavesi et al. (2016, 2018) find that 86% ± 5% and 84% ± 4% of the [C II] emission come from PDRs based on their [C II]/[N II] line ratios, respectively. Thus, we here assume a neutral fraction of 85% for the [C II] emission in SPT 0452−50, which provides a "neutral" line luminosity ratio of $r_{CIIn,OI} = 5.8 \pm 1.4$, where we increased the uncertainty by 20% to account for the uncertainty in the [C II] neutral fraction. Based on the dust optical depth of SPT 0452−50 at the respective line frequencies, we expect this ratio to only be mildly affected by dust optical depth effects. For a typical radiation field strength G_0 of order 10^3, the models by M. L. Luhman et al. (2003) suggest a PDR density of order ~3–4 × 10^3 cm^{-3} at this line ratio, which is not unusual for star-forming gas.

4.2.3. Is SPT 0452−50 a "Typical" z > 5 DSFG?

Since SPT 0452−50 was an outlier in the relationships between T_{dust}, L_{FIR}, and z in the SPT sample as reported by C. Reuter et al. (2020), we here return to the question if it remains unusual after revising the redshift. In the left panel of Figure 7, the T_{dust}–z relation for all known $z > 5$ DSFGs is shown. The difference in values for some sources compared to the compilation by D. A. Riechers et al. (2020) is due to the updated SED fits for those sources.

The relation shows that the median T_{dust} of known $z > 5$ DSFGs is more similar to Arp 220 (and, thereby, the $z = 6.34$ DSFG HFLS3) than to the Cosmic Eyelash when fit with the same SED code, although 10%–15% of the sample have a T_{dust} close to the Eyelash. This is interesting, because the above

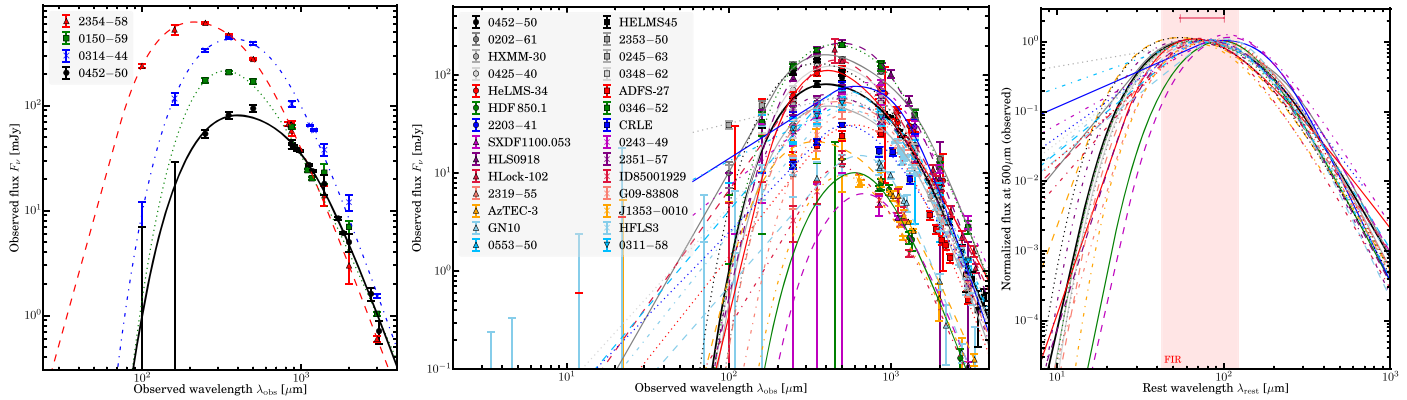

Figure 6. Spectral energy distributions of the "confirmed" sample (left; symbols) and $z > 5$ DSFGs (middle/right) and MBB SED fits (lines; Tables 5 and 6) to the data. Left and middle: observed-frame apparent fluxes. SPT 0452−50 is shown in both panels for reference. Right: 500 μm normalized rest-frame models ($z > 5$ sample only). The shaded region indicates the far-infrared luminosity range. The top bar indicates the range in peak wavelengths.

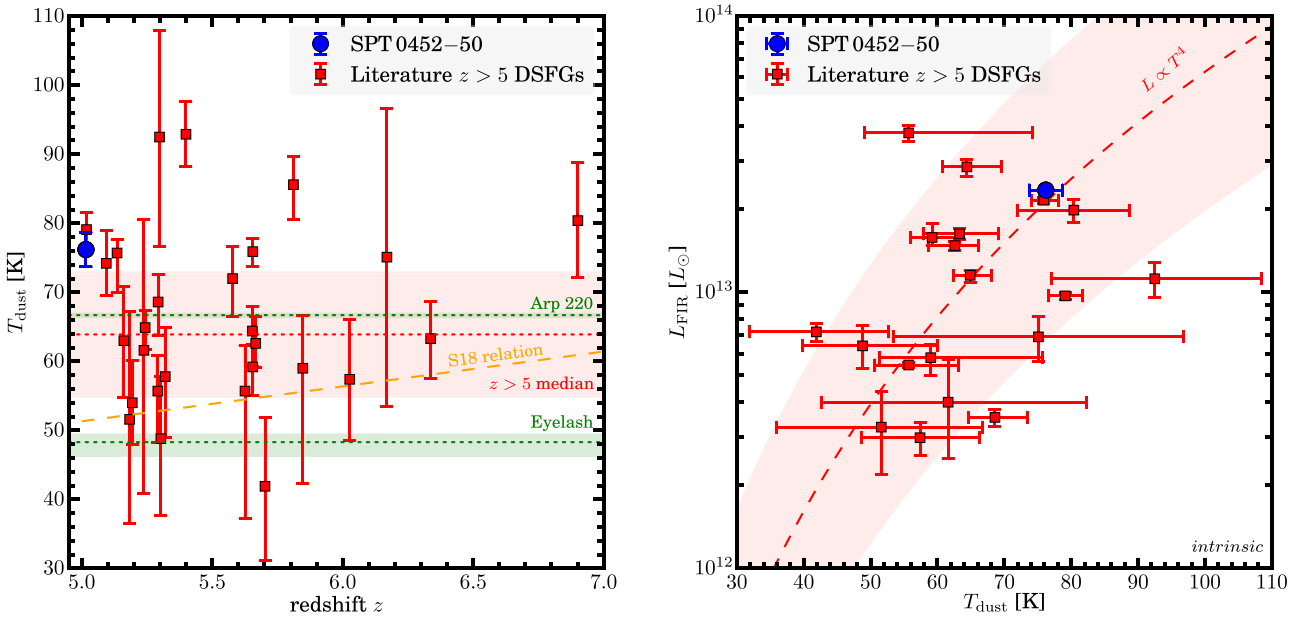

Figure 7. T_{dust}–redshift relation (left) and T_{dust}–L_{FIR} relation (right), updated from D. A. Riechers et al. (2020). Only sources with reliable magnification factors are included in the right panel, and corrected correspondingly. Left: for reference, the median redshift of the sample and the values for the dusty starbursts Arp 220 and the Eyelash are shown as dotted lines, where the shaded regions indicate the median absolute deviation and 1σ uncertainties, respectively. In addition, the scaling relation proposed by C. Schreiber et al. (2018) is shown as a dashed line. Right: a standard $L \propto T^4$ scaling, normalized to the sample median, is shown for reference as a dashed line, with a ±0.5 dex range added as a shaded region.

sources are commonly used as SED templates for finding the most distant DSFGs. While there is no obvious trend of T_{dust} with z within the sample, we also find that the revised median T_{dust} appears consistent with the T_{dust}–z trend proposed by C. Schreiber et al. (2018), but we caution that the SED fitting methods differ.

In the right panel of Figure 7, the relationship between T_{dust} and L_{FIR} is shown for the same sample. This panel contains fewer points, because sources with unknown lensing magnification factors were removed. With the updated SED fits compared to previous work, the trend is even more consistent with a standard $L \propto T^4$ scaling relation.

In combination, these relations show that SPT 0452−50 is a rather "typical" $z > 5$ DSFG among the known specimens, where its higher-than-average T_{dust} can be entirely explained by its relatively high intrinsic L_{FIR}. As such, it is no longer an outlier, and most certainly not an unusually cold starburst.

4.2.4. A z > 5 DSFG SED Template

The median (average) redshift of the full $z > 5$ DSFG sample is 5.36 ± 0.27 (5.52 ± 0.44), where the uncertainties are the median absolute deviation and the standard deviation, respectively. Based on our analysis, we provide a median SED template for $z > 5$ DSFGs, with the parameters $T_{dust} = 63.9 \pm 9.0$ K, β_{IR}=2.52 ± 0.21, $\lambda_{peak} = 73 \pm 8$ μm, and $\lambda_0 = 189 \pm 31$ μm in the rest frame. A corresponding average-based SED template would take the form $T_{dust} = 66.6 \pm 12.7$ K, $\beta_{IR} = 2.41 \pm 0.43$, $\lambda_{peak} = 74 \pm 12$ μm, and $\lambda_0 = 185 \pm 47$ μm, which is indistinguishable within the uncertainties. The corresponding median (lensing-corrected) L_{FIR} of the template is $(1.05 \pm 0.56) \times 10^{13}$ $L_\odot$, with an average of $(1.27 \pm 0.95) \times 10^{13}$ $L_\odot$.

A potential fine-tuning of the template could be to add a scaling of T_{dust} with L_{FIR}, of the form $L_{FIR} = aT_{dust}^4$. Scaled to the median, we find $a = 5.80$. We caution that this correction will, of course, not be valid for samples where strong lensing is expected to be a major contributor to the selection.

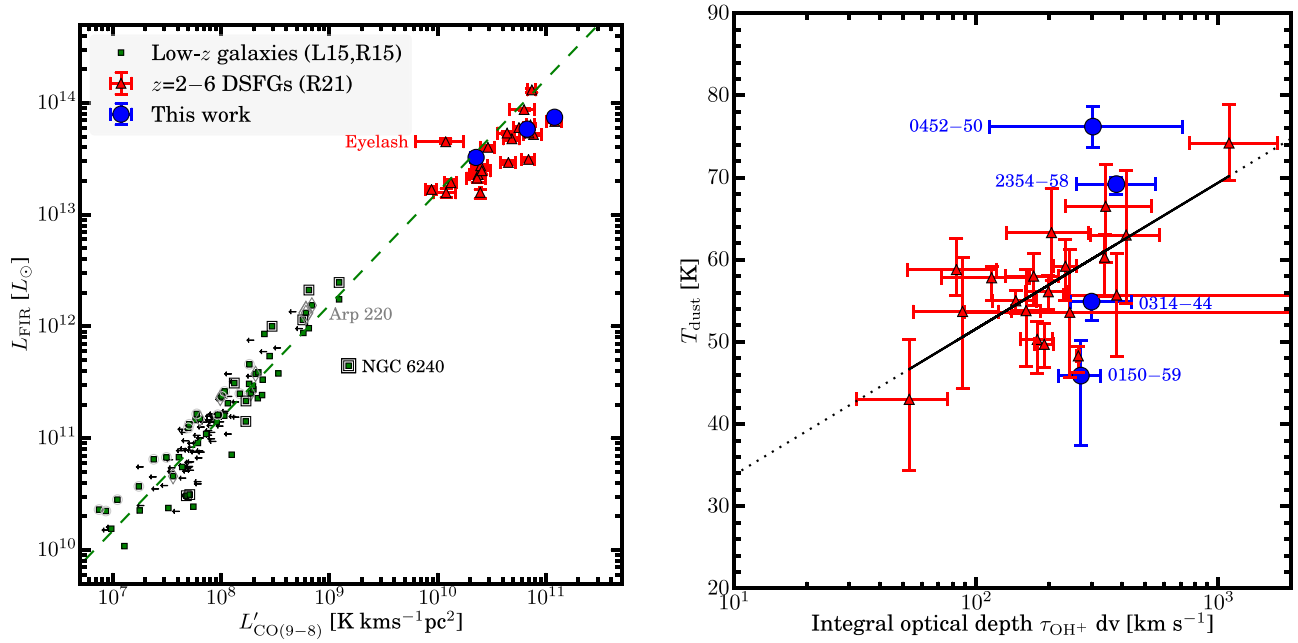

Figure 8. Left: CO($J = 9 \rightarrow 8$)–far-infrared luminosity relation, updated from D. A. Riechers et al. (2021a), including nearby galaxies (green symbols and upper-limit arrows; D. Liu et al. 2015, L15), a high-z DSFG sample from the literature (red triangles; all data from D. A. Riechers et al. 2021a, R21), and the sources reported here (blue dots). The dashed line is the power-law fit to the nearby galaxy sample from L15, with a slope of $N = 1.01$. Luminosities were not corrected for gravitational lensing magnification. Gray circle, diamond, and square outlines indicate Class I, II, and III sources, respectively, where higher classes indicate higher CO excitation (M. J. F. Rosenberg et al. 2015, R15). Right: relation (black line) between the dust temperature and the OH^+ integral optical depth, with the same marker styles, updated from D. A. Riechers et al. (2021a). The relation has the functional form $T_{dust} = a + 1\ \mathrm{K} \log(b\ \tau_{OH+}\mathrm{dv})$, where $a = (16.0 \pm 12.5)$ K and $b = (7.7 \pm 2.3)(\mathrm{km\ s^{-1}})^{-1}$.

4.3. New Constraints on the Gas Properties of SPT-selected DSFGs

4.3.1. CO(J = 9 → 8)–L_{FIR} Relation

D. A. Riechers et al. (2021a) have found a strong correlation between the CO($J = 9 \rightarrow 8$) and far-infrared dust continuum luminosities for a sample of 20 highly luminous, Herschel-selected starburst galaxies at $z = 2$–6 and the Cosmic Eyelash at $z = 2.3$, consistent with the idea that the CO($J = 9 \rightarrow 8$) emission is associated with warm and dense molecular gas in the star-forming regions. The three SPT-selected galaxies with detections reported here fall within the scatter of the Herschel sample, and thus appear indistinguishable in their properties for this relation (Figure 8, left). As such, the combined sample appears systematically offset toward higher CO($J = 9 \rightarrow 8$) luminosity when compared to nearby star-forming galaxies, strengthening the trend reported by D. A. Riechers et al. (2021a). As explained by these authors, this is likely either due to increased shock excitation, increased cosmic-ray energy densities, or a combination of both effects.

4.3.2. T_{dust}–OH^+ Opacity Relation

D. A. Riechers et al. (2021a) have also reported an apparent relation between the dust temperature and OH^+ integrated optical depth $\tau_{OH+}dv$ for the same sample of Herschel-selected sources. This relation is likely related to an underlying relation between T_{dust} and the star formation rate surface density, Σ_{SFR}, which yields an increased cosmic-ray energy density in more compact, warmer sources due to a higher supernova density. Since higher cosmic-ray fluxes increase the OH^+ ion abundance, this then can lead to an increase in OH^+ absorption strength.

For the two new SPT sources where both OH^+ $1_1 \rightarrow 0_1$ and $1_2 \rightarrow 0_1$ have been detected, we find that the $\tau_{OH+}dv$ between both lines are indistinguishable within the uncertainties, consistent with what has been reported by D. A. Riechers et al. (2021a). As such, we also include SPT 0452−50 in this analysis, where only the $1_2 \rightarrow 0_1$ transition has been measured. Three of the SPT galaxies lie within the scatter of the previous data points, with the lowest signal-to-noise detection SPT 0452−50 showing the largest distance from the trend. The modest increase in sample size neither substantially strengthens nor weakens the previous trend (Figure 8, right).

The average column density of $N(OH^+)$ of $(1.5 \pm 0.2) \times 10^{15}$ cm^2 for the new sources is consistent with the median reported for the larger sample studied by D. A. Riechers et al. (2021a). Combining both samples, we find a revised median value of $(1.1 \pm 0.4) \times 10^{15}$ cm^2, which corresponds to a median atomic hydrogen column density of $(7.2 \pm 2.2) \times 10^{22}$ cm^2.

4.3.3. Comparing NH and OH^+ Absorption

NH(N_J=$1_2 \rightarrow 0_1$) was previously detected in absorption in the $z = 2.95$ DSFG HerBS-89a, and in emission in the $z = 3.39$ DSFG Orochi (S. Berta et al. 2021; D. A. Riechers et al. 2021a). The absorption lines detected here toward SPT 0150–59 and 0314–44 show ~20%–40% of the integrated optical depth of OH^+($N_J = 1_2 \rightarrow 0_1$), which is similar to the ~20% seen in HerBS-89a. Given the modest optical depths seen for both species, the difference in line strengths between NH and OH^+ is likely a good indicator of the difference in abundances of both molecules in the same environments.

5. Conclusions

We have targeted the CO($J = 9 \rightarrow 8$) and OH^+($N_J = 1_1 \rightarrow 0_1$) line in the four millimeter-selected, high-redshift

DSFGs SPT 2354−58, 0150−59, 0314−44, and 0452−50. For the first three sources we independently confirm their redshifts, and find line and dust continuum properties consistent with the relations between CO($J = 9 \rightarrow 8$) luminosity and far-infrared luminosity and between the OH^+ integral optical depth and dust temperature proposed by D. A. Riechers et al. (2021a). These findings are consistent with the presence of dust-enshrouded starbursts permeated by a high cosmic-ray energy density leading to high CO($J = 9 \rightarrow 8$) luminosities and OH^+ abundances, with a possible contribution by increased shock excitation to the CO line ladder.

Based on a serendipitous [O I]($^3P_0 \rightarrow {}^3P_1$) detection in these data, and in combination with follow-up, archival, and literature data, we also find that the last source, SPT 0452−50, is not an unusually cold massive starburst at $z = 2.011$ as previously thought, but rather a hyperluminous massive $z = 5.016$ starburst with properties typical for this population.

We analyze SPT 0452−50 in concert with the known $z > 5$ dusty starburst population, and propose a simple dust SED template which may be useful for the identification of more such systems at $z > 5$, and for the extraction of physical properties for similar systems with limited photometry.

Our analysis does not provide evidence for the existence of unusually cold starburst galaxies in the early Universe, which could have been missed by some of the standard selection techniques. While they may still exist, it remains unclear if they are a major source of bias for the study of $T_{\rm dust}$–z relations for dust-selected samples.

Acknowledgments

The author thanks the anonymous referee for a helpful report. D.R. gratefully acknowledges support from the Collaborative Research Center 1601 (SFB 1601 subprojects C1, C2, C3, and C6) funded by the Deutsche Forschungsgemeinschaft (DFG) – 500700252. This work makes use of the following ALMA data: ADS/JAO.ALMA# 2023.1.01481.S, 2021.2.00062.S, 2019.1.00297.S, 2019.1.01026.S, 2016.1.00231.S, 2011.0.00957.S, and 2011.0.00958.S. ALMA is a partnership of ESO (representing its member states), NSF (USA) and NINS (Japan), together with NRC (Canada) and NSC and ASIAA (Taiwan), in cooperation with the Republic of Chile.

Facility: ALMA.

ORCID iDs

Dominik A. Riechers https://orcid.org/0000-0001-9585-1462

References

Aravena, M., Spilker, J. S., Bethermin, M., et al. 2016, MNRAS, 457, 4406
Berta, S., Young, A. J., Cox, P., et al. 2021, A&A, 646, A122
Bialy, S., Neufeld, D., Wolfire, M., Sternberg, A., & Burkhart, B. 2019, ApJ, 885, 109
Blain, A. W., Smail, I., Ivison, R. J., Kneib, J. P., & Frayer, D. T. 2002, PhR, 369, 111
Butler, K. M., van der Werf, P. P., Rybak, M., et al. 2021, ApJ, 919, 5
Carilli, C. L., & Walter, F. 2013, ARA&A, 51, 105
Combes, F., Rex, M., Rawle, T. D., et al. 2012, A&A, 538, L4
Cox, P., Neri, R., Berta, S., et al. 2023, A&A, 678, A26
Dowell, C. D., Conley, A., Glenn, J., et al. 2014, ApJ, 780, 75
Dudzevičiūtė, U., Smail, I., Swinbank, A. M., et al. 2020, MNRAS, 494, 3828
Fudamoto, Y., Ivison, R. J., Oteo, I., et al. 2017, MNRAS, 472, 2028
González-Alfonso, E., Fischer, J., Graciá-Carpio, J., et al. 2012, A&A, 541, A4
Gururajan, G., Bethermin, M., Sulzenauer, N., et al. 2023, A&A, 676, A89
Hezaveh, Y. D., Marrone, D. P., Fassnacht, C. D., et al. 2013, ApJ, 767, 132
Hodge, J. A., & da Cunha, E. 2020, RSOS, 7, 200556
Hollenbach, D., Kaufman, M. J., Neufeld, D., Wolfire, M., & Goicoechea, J. R. 2012, ApJ, 754, 105
Ikarashi, S., Ivison, R. J., Cowley, W. I., & Kohno, K. 2022, A&A, 659, A154
Indriolo, N., Bergin, E. A., Falgarone, E., et al. 2018, ApJ, 865, 127
Ismail, D., Beelen, A., Buat, V., et al. 2023, A&A, 678, A27
Jin, S., Daddi, E., Magdis, G. E., et al. 2019, ApJ, 887, 144
Liu, D., Gao, Y., Isaak, K., et al. 2015, ApJL, 810, L14
Luhman, M. L., Satyapal, S., Fischer, J., et al. 2003, ApJ, 594, 758
Magnelli, B., Lutz, D., Saintonge, A., et al. 2014, A&A, 561, A86
McMullin, J. P., Waters, B., Schiebel, D., Young, W., & Golap, K. 2007, in ASP Conf. Ser. 376, Astronomical Data Analysis Software and Systems XVI, ed. R. A. Shaw, F. Hill, & D. J. Bell (San Francisco, CA: ASP), 127
Mitsuhashi, I., Harikane, Y., Bauer, F. E., et al. 2024, ApJ, 971, 161
Pavesi, R., Riechers, D. A., Capak, P. L., et al. 2016, ApJ, 832, 151
Pavesi, R., Riechers, D. A., Sharon, C. E., et al. 2018, ApJ, 861, 43
Planck Collaboration, Abergel, A., Ade, P. A. R., et al. 2011, A&A, 536, A25
Rawle, T. D., Egami, E., Bussmann, R. S., et al. 2014, ApJ, 783, 59
Reuter, C., Vieira, J. D., Spilker, J. S., et al. 2020, ApJ, 902, 78
Riechers, D. A., Bradford, C. M., Clements, D. L., et al. 2013, Natur, 496, 329
Riechers, D. A., Capak, P. L., Carilli, C. L., et al. 2010, ApJL, 720, L131
Riechers, D. A., Carilli, C. L., Capak, P. L., et al. 2014, ApJ, 796, 84
Riechers, D. A., Cooray, A., Pérez-Fournon, I., & Neri, R. 2021a, ApJ, 913, 141
Riechers, D. A., Hodge, J. A., Pavesi, R., et al. 2020, ApJ, 895, 81
Riechers, D. A., Leung, T. K. D., Ivison, R. J., et al. 2017, ApJ, 850, 1
Riechers, D. A., Nayyeri, H., Burgarella, D., et al. 2021b, ApJ, 907, 62
Rosenberg, M. J. F., van der Werf, P. P., Aalto, S., et al. 2015, ApJ, 801, 72
Schreiber, C., Elbaz, D., Pannella, M., et al. 2018, A&A, 609, A30
Spilker, J. S., Marrone, D. P., Aravena, M., et al. 2016, ApJ, 826, 112
Strandet, M. L., Weiss, A., De Breuck, C., et al. 2017, ApJL, 842, L15
Strandet, M. L., Weiss, A., Vieira, J. D., et al. 2016, ApJ, 822, 80
Tamura, Y., Mawatari, K., Hashimoto, T., et al. 2019, ApJ, 874, 27
Vieira, D., Riechers, D. A., Pavesi, R., et al. 2022, ApJ, 925, 174
Vieira, J. D., Crawford, T. M., Switzer, E. R., et al. 2010, ApJ, 719, 763
Walter, F., Decarli, R., Carilli, C., et al. 2012, Natur, 486, 233
Weiß, A., De Breuck, C., Marrone, D. P., et al. 2013, ApJ, 767, 88
Yang, C., Omont, A., Beelen, A., et al. 2016, A&A, 595, A80
Zavala, J. A., Montaña, A., Hughes, D. H., et al. 2018, NatAs, 2, 56